Midinfrared one-dimensional photonic crystal constructed from two-dimensional electride material

Liwei Zhang,[1] Weiyang Yu,[1,2] Jun-Yu Ou,[3] Qin Wang,[1] Xiaolin Cai,[1,2] Baoji Wang,[1] Xiaohua Li,[1] Ruiqi Zhao,[4] and Yujin Liu[1,*]

[1]*School of Physics and Electronic Information Engineering, Henan Polytechnic University, Jiaozuo, Henan 454000, People's Republic of China*

[2]*International Laboratory for Quantum Functional Materials of Henan, Zhengzhou University, Zhengzhou 450001, People's Republic of China*

[3]*Optoelectronics Research Centre and Centre for Photonic Metamaterials, University of Southampton, Southampton SO17 1BJ, England, United Kingdom*

[4]*School of Materials Science and Engineering, Henan Polytechnic University, Jiaozuo, Henan 454000, People's Republic of China*

(Received 31 May 2018; revised manuscript received 25 July 2018; published 28 August 2018)

Dicalcium nitride (Ca_2N) is a layered material that has been recently identified as a two-dimensional electride, based on first-principles calculations, where the electronic property and the optical complex dielectric function are studied using density functional theory. We find that the optical permittivity tensor is highly anisotropic, and Ca_2N possesses metallic characters when the in-plane dielectric function is negative in midinfrared frequency. In addition, the enhanced midinfrared transmission property and the field distribution of one-dimensional photonic crystals composed of alternating Ca_2N layers and the dielectric material are theoretically studied using the transfer-matrix method. It is found that the Ca_2N photonic crystals support a series of passbands and stopbands the numbers of which increase with the thickness and the permittivity of the dielectrics. The field distributions show that the transmission resonances in the passband are attributed to the coupled Fabry-Pérot resonances of the individual reactively loaded dielectric slabs. It is also noticed that these resonances lie within certain characteristic frequency bands which are independent of the period of the photonic crystal. The low-frequency edge of the passband is highly tunable by the thickness of the electride material and the dielectric material, the permittivity of the dielectric layer, while the high-frequency edge is insensitive to the electride material thickness. Moreover, the first band gap in lower frequency is almost omnidirectional and polarization insensitive. When defect layers are introduced, the twin defect modes are found, and the frequency and the frequency interval of the two defect modes can be tuned just by changing the permittivity, the thickness and the position of the defect layer, respectively. Polarization and angular insensitive absorption bands can also be obtained for the electride-dielectric photonic crystal with a reflective substrate. These properties of electride material photonic crystals have potential applications in tunable multiband filters and absorbers in the midinfrared region.

DOI: 10.1103/PhysRevB.98.075434

I. INTRODUCTION

Electrides are a class of materials where electrons perform the same function as anions [1]. These electrons are spatially confined and separated from the cations in the crystal and are not bound to any particular lattice site. According to the dimensionality of the anionic confined region, electrides can be classified as zero-dimensional, one-dimensional (1D), and two-dimensional (2D). Some electrides crystallize in a layered structure [2–4], in which anionic electrons are found in 2D planes, where the proximity of the anionic electrons causes them to partially delocalize as 2D electron gas. Recently, a new type of electrides with 2D confinement of anionic electrons was discovered in Ca_2N [3]. First-principles calculations have also predicted several other 2D electrides, including Sr_2N, Ba_2N, etc. [5]. As a 2D electride in terms of $[Ca_2N]^+e^-$, Ca_2N offers exciting properties such as high electrical conductivities and highly anisotropic optical response with metallic character. A Ca_2N layer effectively behaves as a "metal" layer capable of supporting a p-polarization surface-plasmon polariton [6] which shows similar behavior to that in noble metals [7] and some van der Waals materials [8]. Recently, it was found that the photonic crystals (PCs) containing metalliclike materials and dielectrics possess special transmission properties [9–11].

Photonic crystals [12,13], which can be constructed in 1D, 2D, and three-dimensional (3D) periodic structures, are artificially designed to control and manipulate the interaction of light with matter. The essential property of PCs is the photonic band-gap structure; some applications based on PCs, such as sensors, absorber, filters, high-Q cavities, etc., have been proposed [12–16]. One-dimensional PCs are of particular interest due to their easy fabrication processes and practical applications in layered optical systems, and the optical characteristics can be manipulated by tuning the periodicity and the thickness of the constitute layers. For the 1D metal-dielectric stack, although extremely thin metal layers are highly reflective, the superposition of a number of these layers separated by optically thick transparent dielectric slabs has been shown to generate high transmissivity bands

*wflyj@hpu.edu.cn

within a characteristic band in the visible region [9]. Recently, microwave transmissivity of a metamaterial-dielectric stack has been investigated [17,18], where the metal film is designed on the subwavelength scale to create a metamaterial with effective Drude-like electromagnetic properties. The transmission property and field distribution in 1D graphene-dielectric structures are also studied in low-terahertz frequencies [10,19]. The spectra for such metalliclike material multilayer structures consist of a series of passband and stopband regions and the corresponding resonances of transmission within the passband are explained in terms of coupled Fabry-Pérot (FP) resonances [11]. However, to our knowledge the similar enhanced transmission properties have not been studied yet in midinfrared with an anisotropic metallic reflectivity mirror, such as a natural 2D electride. The recent electronic and optical property studies about electrides [2–6] demonstrated that electrides possess excellent metal-like characteristics; the effective negative permittivity cutoff frequency is in midinfrared. The *p*-polarization surface-plasmon polariton supported by electrides has been theoretically studied [6], and is similar to a metal in optical frequency [7,20] and graphene in low-terahertz ranges [21]. In this paper, the detailed optical characteristics of the 1D Ca_2N-dielelctric PCs, such as enhanced transmission, field distribution, defect modes, and absorption properties, are investigated theoretically.

II. MODEL AND COMPUTATIONAL DETAILS

For the electronic and optical properties of Ca_2N, the density-functional theory (DFT) calculations are performed with the Vienna Ab Initio Simulation Package code [22]. The projector-augmented wave method [23] is applied to describe the electron-ion interactions. The exchange-correlation energy is described by the generalized gradient approximation using the Perdew-Burke-Ernzerhof (PBE) functional [24]. Plane waves with a kinetic energy cutoff of 600 eV are used to expand the wave functions and the convergence criteria for energy and force are set to be 10^{-5} eV and 0.01 eV/Å, respectively. DFT-D2 method is applied to describe the long-range van der Waals interaction [25]. The Brillouin zone is sampled by a Gamma-centered $21 \times 21 \times 3$ Monkhorst-Pack k-point mesh for the geometry optimization and static electronic structure calculation. For optical permittivity calculations, the k point is enlarged to $41 \times 41 \times 9$ to ensure a sufficient description of the optical permittivity, and the Brillouin-zone integrations are performed using the first-order Methfessel-Paxton method [26] with a width of 0.1eV. Optical properties are some of the most important properties for a material, indicating a material's response to electromagnetic radiation. To model the optical response of Ca_2N, which possesses a metallic property, we calculate the frequency dependent dielectric function, consisting of interband and intraband contributions, $\varepsilon(\omega) = \varepsilon_{\text{inter}}(\omega) + \varepsilon_{\text{intra}}(\omega)$, which are obtained separately. The imaginary part of the interband contribution $\varepsilon_{\text{inter}}(\omega)$ involves the interband matrix elements of the momentum operators, and can be evaluated directly in DFT. The real part of the dielectric function can be obtained by the usual Kramers-Kronig transformation. The intraband contribution $\varepsilon_{\text{intra}}(\omega)$ is usually modeled by a free-electron Drude model, which contains a plasma frequency tensor ω_{p} calculated from first principles. The corresponding intraband contribution to the permittivity is $\varepsilon_{\text{intra}}(\omega) = 1 - \omega_p^2/(\omega^2 + \Gamma^2) + i\Gamma\omega_p^2/(\omega^3 + \omega\Gamma^2)$ [7], where Γ is a lifetime broadening obtained either from a higher-order calculation or from experiments. In our calculations, we used the experimentally determined electron lifetime (0.6 ps) for bulk Ca_2N to estimate Γ [3]. Since Ca_2N is of typical layered structure, its dielectric properties are expected to exhibit intrinsic anisotropy.

One-dimensional PCs containing alternating 2D electride material A (such as Ca_2N film) and dielectric B along the z axis in air background are considered, as shown in the inset of Fig. 3(c). The dimensions in the x and y directions are assumed to be infinite; a plane wave is incident from the vacuum at an angle θ onto the 1D PC. The electride A is separated by dielectric layers B with thickness d_b and relative permittivity ε_b, and N is the number of the period. The period of the layered structure is $d = d_a + d_b$, where d_a is the electride material thickness. Since Ca_2N is anisotropic, the permittivity ε_A is a tensor. For simplicity, we assume $\mu_A = 1$ and the ε_A tensor is simultaneously diagonalizable, $\varepsilon_A = \text{diag}[\varepsilon_{xx}, \varepsilon_{yy}, \varepsilon_{zz}]$, which can be calculated from DFT. We consider the oblique monochromatic incident plane wave propagating along the z axis with the electric field and magnetic field polarized along the y axis for the TE and TM waves, respectively. For the TE mode, the electric and magnetic fields can be expressed as

$$\begin{aligned} E_{Ay} &= e^{ik_x x}(A'e^{ik_{Az}z} + B'e^{-ik_{Az}z}), \\ H_{Ax} &= \frac{-k_{Az}}{\omega\mu_0\mu_A} e^{ik_x x}(A'e^{ik_{Az}z} - B'e^{-ik_{Az}z}), \\ H_{Az} &= \frac{k_x}{\omega\mu_0\mu_A} e^{ik_x x}(A'e^{ik_{Az}z} + B'e^{-ik_{Az}z}) \end{aligned} \tag{1}$$

in electride material layer A, and

$$\begin{aligned} E_{By} &= e^{ik_x x}(Ce^{ik_{Bz}z} + De^{-ik_{Bz}z}), \\ H_{Bx} &= \frac{-k_{Bz}}{\omega\mu_0\mu_B} e^{ik_x x}(Ce^{ik_{Bz}z} - De^{-ik_{Bz}z}), \\ H_{Bz} &= \frac{k_x}{\omega\mu_0\mu_B} e^{ik_x x}(Ce^{ik_{Bz}z} + De^{-ik_{Bz}z}) \end{aligned} \tag{2}$$

in dielectric layers B, where $k_{Az}^2 = \omega^2\varepsilon_{Ay}\mu_A/c^2 - k_x^2$ and $k_{Bz}^2 = \omega^2\varepsilon_B\mu_B/c^2 - k_x^2$, where k_{A_z} and k_{B_z} are the z components of the wave vector in each layer, and $k_x = k_0 \sin\theta$ is the tangential component of the wave vector [27], which is equal to that of the incident wave. A', B', C, and D are four constants which can be determined by the boundary conditions at the interfaces. For a finite periodic structure, the electric and magnetic fields at any two positions z and $z + \Delta z$ in the same layer can be related via a transfer matrix [28]:

$$M_{A,B} = \begin{pmatrix} \cos(k_{A,Bz}d_{a,b}) & i\frac{\mu_{A,B}\omega}{k_{A,Bz}c}\sin(k_{A,Bz}d_{a,b}) \\ i\frac{k_{A,Bz}c}{\mu_{A,B}\omega}\sin(k_{A,Bz}d_{a,b}) & \cos(k_{A,Bz}d_{a,b}) \end{pmatrix}. \tag{3}$$

By means of the transfer-matrix method, we can obtain the transmission coefficient of a monochromatic plane wave, $t(\omega) = \frac{2p_0}{[p_0 x_{22}(\omega) + p_s x_{11}(\omega)] - [p_0 p_s x_{12}(\omega) + x_{21}(\omega)]}$, where $p_0 = p_s = \cos\theta$ for the air background and $x_{ij}(i, j = 1, 2)$ are the

matrix elements of $X(\omega) = \prod M_{A,B}$, which represents the total transfer matrix connecting the fields at the incident end and the exit end. The treatment for the TM wave is similar, where $k_{Az}^2 = \omega^2 \varepsilon_{Ax}\mu_A/c^2 - \varepsilon_{Ax}/\varepsilon_{Az}k_x^2$.

For the TE mode case, based on Bloch's theorem and the boundary condition, the dispersion relation for any incident angle is as follows [29]:

$$\cos(\beta d) = \cos(k_{Az}d_A + k_{Bz}d_B) - \frac{1}{2}\left(\frac{k_{Bz}\mu_A}{k_{Az}\mu_B} + \frac{k_{Az}\mu_B}{k_{Bz}\mu_A} - 2\right) \times \sin(k_{Az}d_A)\sin(k_{Bz}d_B). \quad (4)$$

Similarly, the dispersion relation for the TM mode can also be obtained. In Eq. (4), β is the z component of Bloch wave vector, where Bloch waves are propagating for real β and complex β indicates the presence of band gaps.

III. NUMERICAL RESULTS AND DISCUSSIONS

Ca_2N crystallizes in the layered anti-$CdCl_2$ structure with space group R-3m; a 3D crystal is formed by stacking the Ca-N-Ca weakly bonded triple layers along the c axis as shown in Fig. 1(a). In the conventional hexagonal unit cell, three Ca_2N units are stacked, while the primitive rhombohedral unit cell contains one formula unit. It was proposed to have metallic 2D excess electrons in the interlayer gap between the calcium layers both by DFT calculations and by angle-resolved photoemission spectroscopy measurements [30]. Ca_2N behaves like metal with the chemical formula $[Ca_2N]^+e^-$, however the electronic charge is expected to behave rather differently both from the standard metallic bonding [31], where free conduction electrons are shared between the cations, and from the regular ionic compounds. Recently it has been predicted that single- or few-layer Ca_2N can be exfoliated and may behave as a good electronic or battery electrode material [32]. Here we focus on the electronic and optical properties of bulk Ca_2N and the composited structure. We obtain the optimized lattice constants $a = 3.548$ Å and $c = 18.863$ Å by using first-principles calculations based on DFT, which agree well with the experimental values ($a = 3.62$ Å and $c = 19.10$ Å) [33] and other theoretical results [34].

The electronic property can be used to determine the metallic, semiconducting, or insulating character of a material. In metallic materials there is no energy gap between the valance band and conduction band, which can be deduced from the band structure and density of states (DOS). Figures 2(a) and 2(b) display the calculated band structure and DOS profiles using DFT, respectively, where the zero of the energy is the Fermi level (E_F). The first Brillouin zone with symmetry points labeled is shown in Fig. 1(b), where the dashed line marks the primitive unit cell. The electronic band structure displays a single dispersive band (with red color) crossing E_F with its bottom located about -1.56 eV, which shows that Ca_2N possesses metallic property. The DOS can provide more information about the electronic structure. From Fig. 2(b), it is shown that a broad density-of-states peak around E_F appears (clear in the inset) with small contributions from the atomic orbitals of Ca and N, as shown in the projected density-of-states results. And the DOS should mainly come from the excess electrons in the interstitial regions, which cannot be projected onto atomic orbital characters [30]. The band that crosses E_F can be seen to be a 2D band confined within the gap between the Ca layers, which is from the excess electrons. The electrons mostly distribute in the interlayer regions and partially delocalize to form 2D electron gas as illustrated in Fig. 1(a), where the partial electron densities for states within 0.1 eV around E_F are plotted. It is also found that the states near E_F are weakly hybridized with p states of N although the band dispersion is free-electron-like.

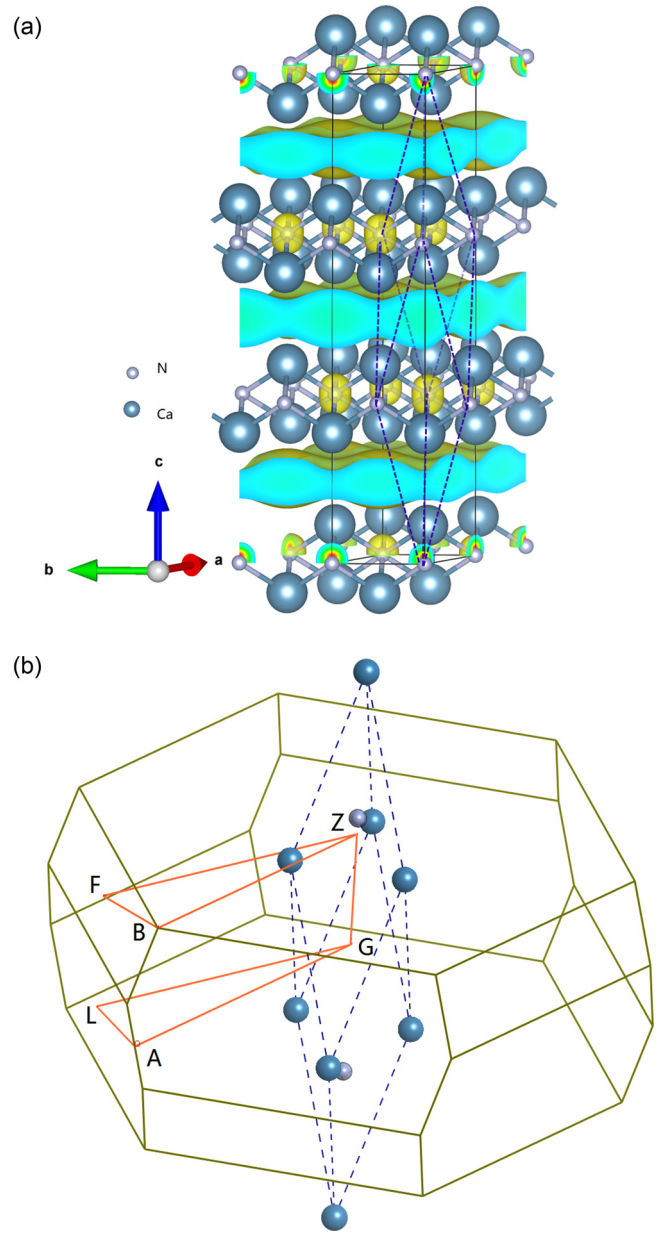

FIG. 1. (a) Plot of the electron-density distributions for states around E_F (within an energy window of 0.1 eV), which shows the anionic electrons distributed between the Ca-N-Ca triple layers; the value of isosurfaces is 0.0006/bohr^3; the solid line marks the conventional unit cell; the large and small spheres denote Ca and N ions, respectively. (b) Brillouin zone with symmetry points labeled; the dashed line marks the primitive unit cell.

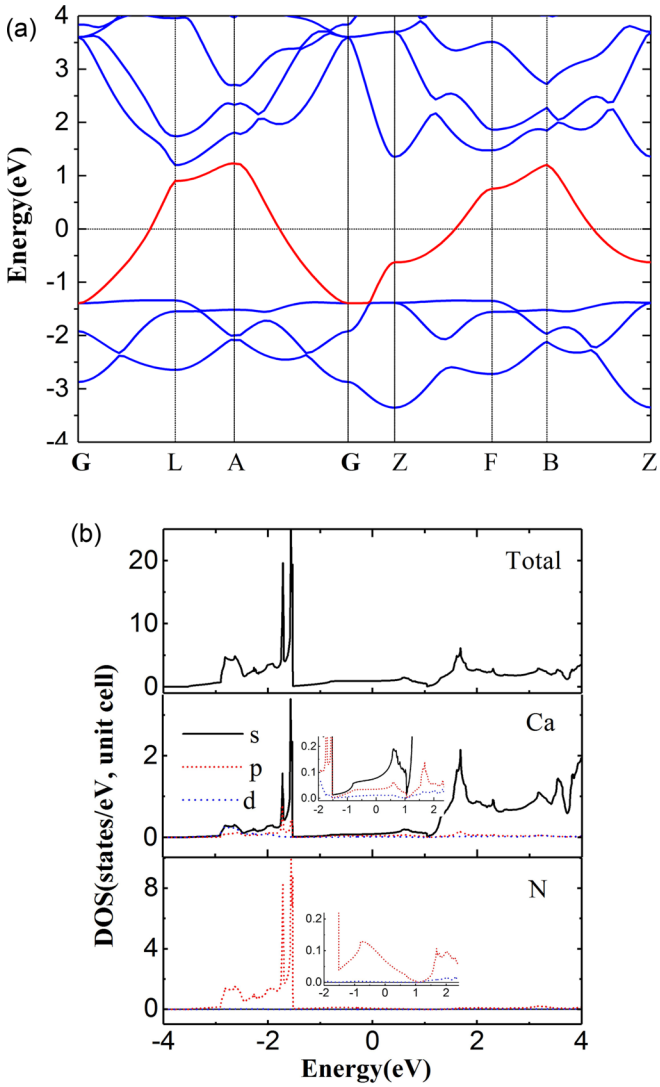

FIG. 2. (a) Electronic band structure of bulk Ca_2N. The band that crosses E_F is from the anionic electrons mostly distributed in the interlayer regions [as shown in Fig. 1(a)]; the horizontal dotted line indicates the E_F. (b) Total and partial density of states.

For the layered electrides, the band is highly dispersive in the x-y plane and less dispersive along the z direction as shown in Fig. 2(a), indicating that these anionic electrons are much more free to move in the interlayer region than to move across the triple layers. Such exceedingly strong electronic anisotropy underlies the appearance of indefinite permittivity over a wide range spectrum, implying a highly anisotropic optical response. As a consequence, Ca_2N behaves as a metal and the dielectric function (ω) exhibits strong anisotropy, which gives rise to exciting optical properties like hyperbolicity and surface plasmons at midinfrared frequencies [4]. Due to the D_{3d} point group symmetry, the permittivity tensor has only two independent elements $\varepsilon_{xx}(\omega)$ and $\varepsilon_{zz}(\omega)$ for the in-plane and out-of-plane components, which is similar to that in a very thin gold thin film [7]. Since Ca_2N behaves like a kind of metal, it has a plasma frequency tensor to describe its permittivity. As we know, some simple metals such as Au, Ag, and Al generally have a large isotropic bulk plasma frequency around 10 eV. Because the electronic charge in Ca_2N is rather different from the standard metallic bonding in metal, and the conducting electron density is lower, its bulk plasma frequency should be lower than those for simple metals. By using DFT calculations, it is found that bulk Ca_2N has an in-plane intraband plasma frequency $\omega_{pxx} = 4.87 \times 10^{16}$ Hz and an out-of-plane intraband plasma frequency $\omega_{pzz} = 1.51 \times 10^{16}$ Hz, which are close to the calculated results in Ref. [6].

Figure 3(a) shows the real and imaginary parts of the in-plane and out-of-plane dielectric functions for bulk Ca_2N, which consists of interband and Drude-like intraband contributions. It is evident that due to intraband contribution the real part of $\varepsilon(\omega)$ crosses from negative value to positive value with increasing frequency, and Ca_2N exhibits the character of metallic behavior in the low-frequency band. It is interesting that the real part of in-plane dielectric function $\mathrm{Re}\varepsilon_{xx}(\omega)$ changes sign at a frequency of about 294 THz, which is different from 84.8 THz for $\mathrm{Re}\varepsilon_{zz}(\omega)$. The anisotropy character leads to an extended frequency window, in which the two components have different signs, and Ca_2N can work as a natural hyperbolic material [34]. Moreover, it is also found that the loss of Ca_2N is very low in the frequency band (60−300 THz) of interest. The approach based on the hybrid functional combined with the possible many-body effects (like GW band modifications and excitonic effects) is expected to yield a more accurate band structure and dielectric function [35], and there will be some shift in the metallic window of Ca_2N. Although the dielectric function calculated by PBE method is not exactly accurate, it is sufficient for the essential optical property study of the 1D PC containing Ca_2N, and the hybrid functional combined with the possible many-body effects deserves to be investigated in future research. In Fig. 3(b), the reflection and transmission properties of a free-standing Ca_2N film with 40 nm in air are calculated. It can be seen that in midinfrared the transmission and absorption (not show here) are low due to the strong reflection from the metallic surface, so the natural electride Ca_2N behaves similarly to a graphene sheet in low-terahertz frequencies [11], and a metal film in visible frequency [36].

The electride Ca_2N possesses metal property in midinfrared since the real part of the permittivity is negative, which immediately suggests the potential for electride material PCs to get special band structure similar to that in metal-dielectric and graphene-dielectric stacks in corresponding frequencies. In Fig. 3(c), we present a typical transmission response of a PC $A(BA)_N$ consisting of $N+1$ Ca_2N films ($N = 5$ and 7) separated by dielectric layers (Si_3N_4) at normal incidence, where the background is air, the incident angle $\theta = 0$, $d_a =$ 40 nm, $d_b = 600$ nm, $\varepsilon_b = 4$ [37], and the absorption loss of the dielectric has been neglected. From Fig. 3(c), it can clearly be noticed that a deep band gap is followed by a passband, and then a second band gap and passband. This is a periodic series of passband regions separated by a band gap, and there are subresonances in the passband region which will correspond to near-standing-wave resonances within each dielectric cavity, as well as those in metal (graphene)-dielectric multilayers. For comparison, the transmission of $A(BA)_5$ without loss is also plotted, where we do not consider the imaginary part for Ca_2N. It is evident that the loss of Ca_2N causes no other effect on the passband resonance and its spectral position except the obvious absorption effects. It is worth noting that

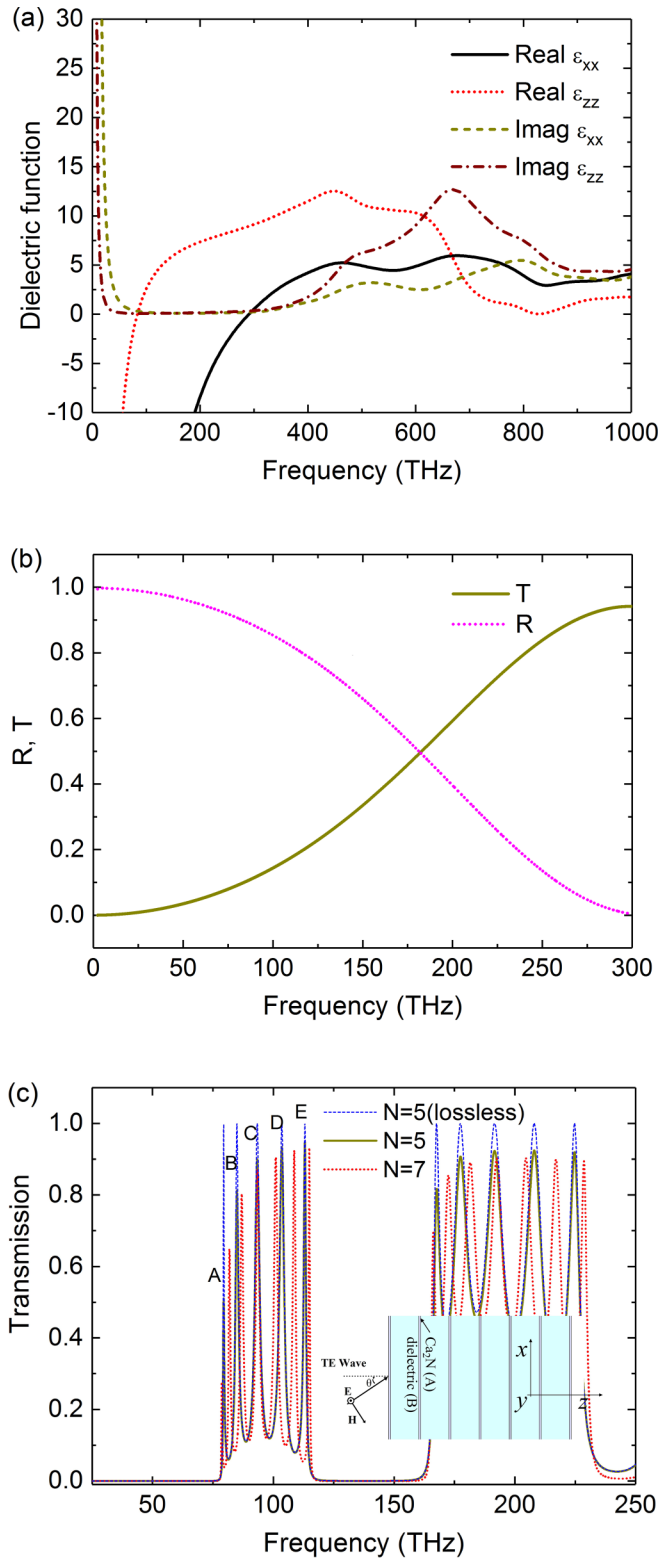

FIG. 3. (a) Real and imaginary parts of the two principal components of permittivity of bulk Ca_2N. (b) Reflectivity and transmission of a Ca_2N film with $d_a = 40$ nm. (c) Transmission of five- and seven-Ca_2N-dielectric stack structures; the inset shows the geometry of a stack $A(BA)_N$, where A represents Ca_2N film with thickness d_a, B denotes a dielectric layer with thickness d_b, and N represents the periodic number, where $\theta = 0$, $d_a = 40$ nm, $d_b = 600$ nm, and $\varepsilon_b = 4$.

each transmission band is composed of a set of N resonant peaks, where N is equal to the number of unit cells in the sample. Although PC theory can be invoked as the underlying mechanism behind this transmission property if the number of unit cells is large, it can be clearly explained by FP resonances for the finite unit cells ($N = 5$ or 7). In the $A(BA)_N$ structure, each unit of Ca_2N-dielectric-Ca_2N forms a FP cavity, and then the multilayer can be treated as a series of coupled FP microcavities, and the coupling between them leads to N resonant peaks in each passband. For the selected modes in the first passband, the component of the wave vector along the z axis is approximately close to $k\pi/(N(d_a + d_b))$, where k is an arbitrary integer [14]. The five resonance peaks at A, B, C, D, and E correspond to the resonant modes with $k = 1$, 2, 3, 4, and 5, respectively. As the number of PC periods increases, the transmission peak number increases, whereas all the peaks lie within a characteristic frequency band. The values of the first and last resonance frequencies tend to some limit values when the periodic number increases. The high frequency band edge at about 115 THz is in agreement with the resonance frequency expected for a single FP etalon when $d_b = 600$ nm, and the resonance frequency can be calculated by using $f = c/(4d_b)$. This suggests that the upper limit could be given by that frequency.

From Fig. 3(c), it is clear that when $N = 7$ the extra layers of Ca_2N slightly increase the overall absorption of the structure, but the position and the bandwidth of the resonance passband are nearly independent of the overall length, which indicates that the band structure depends only on the unit cell of each layer. The model is similar to the studies in Refs. [11,19,38], where the graphene (metamaterial) acts as a tunnel barrier. In what follows, we discuss the properties of the electric-field distributions just in the first passband since these are sufficient to fully understand the structure's fundamental behavior. Figure 4 illustrates the electric field distributions along the $A(BA)_5$ structure in the z direction, where the gray and dark gray indicate the location of the Ca_2N and dielectric layers, respectively. It is clear that for all the five peaks in the first passband [labeled as A, B, C, D, and E in Fig. 3(c)] strong electric fields are concentrated within the $A(BA)_5$ region, but prominent differences exist among them in terms of the distribution profile. For the peak at A ($f = 79.41$ THz), the electric fields in adjacent cavities oscillate in phase and the amplitude of the field is strong within all the five unit cells and there is no field node (where the field amplitudes approach a minimum value) through the whole structure. The field values are relatively small over each of those internal Ca_2N layers for mode E ($f = 113.03$ THz), the field in each dielectric cavity oscillates out of phase with its adjacent cavities, and four field nodes exist in between every two neighboring unit cells. For mode D ($f = 103.49$ THz), there are two Ca_2N layers with low field levels and one field node in the center of the middle dielectric layer. For mode C ($f = 93.33$ THz) and B ($f = 84.90$ THz) no Ca_2N layer has very low electric-field value, while the field in the dielectric cavity oscillates out of or in phase with the other, and there is one field node at the center position of the whole structure for mode B and two field nodes in the second and fourth unit cells for mode C, respectively. It should be noted that the high-frequency edge corresponds to a sequential series of coupled FP cavities, however it occurs

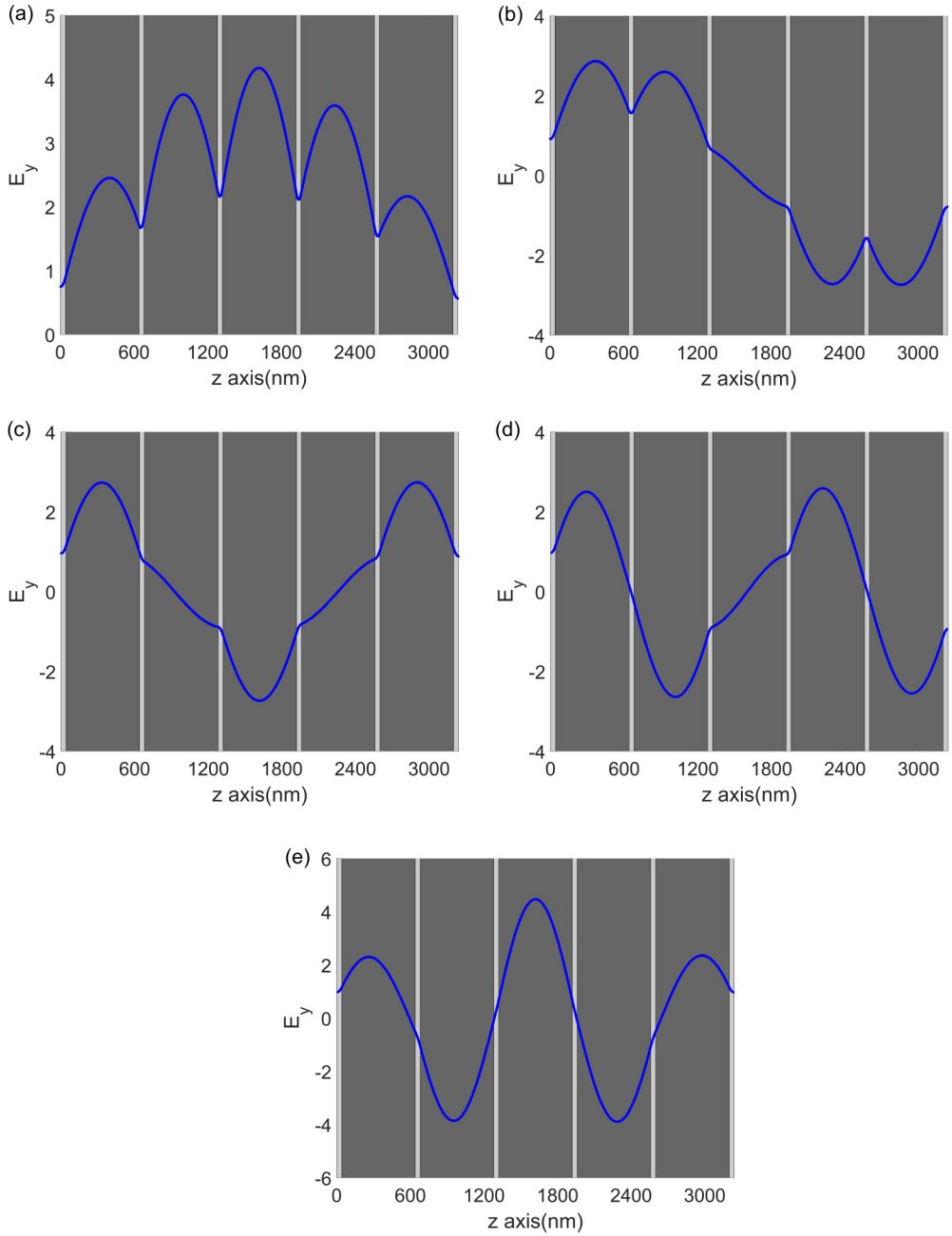

FIG. 4. Electric-field distributions for the five resonance modes A, B, C, D, and E [shown in Fig. 3(c)] in the first passband of the $A(BA)_5$ stack: (a) $f = 79.41$ THz, (b) $f = 84.90$ THz, (c) $f = 93.33$ THz, (d) $f = 103.49$ THz, and (e) $f = 113.03$ THz; the gray and dark gray indicate the locations of the Ca_2N and dielectric layers.

at a lower frequency than 125 THz (i.e., FP etalon limit) due to the finite conductivity of the Ca_2N in the frequency. These well-organized phase profiles reflect the basic features of the hybridization resonances supported by the $A(BA)_5$ structure.

Typical FP resonators are made by using a pair of broadband high reflectivity mirrors, such as metals or distributed Bragg reflectors, and a cavity is filled with a dielectric material. In the present structure, Ca_2N film works as a high reflectivity mirror in midinfrared, and when changing the thickness and the permittivity of dielectric the band structures can be tunable. So increasing the thickness or permittivity of the dielectric more passbands and band gaps in a certain frequency band can be obtained, and the corresponding field distribution in each microcavity will have more resonant peaks and nodes [10]. To demonstrate the properties, a 2D map of transmittance of the 1D multilayer $A(BA)_5$ as a function of incident frequency with different dielectric thickness d_b is illustrated in Fig. 5(a), where $\theta = 0$, $d_a = 40$ nm, and $\varepsilon_b = 4$, respectively. It can clearly be seen that when the thickness of the dielectric equals to about 200 nm the spectrum shows only one passband in midinfrared. As the dielectric layer is 400 nm, a new passband occurs in the region of interest. If we further increase the thickness of the dielectric to 1200 nm, we can obtain more passbands and band gaps in the midinfrared region. Meanwhile, the distance between the two adjacent passbands becomes shorter. But there are still five resonance peaks in every passband as expected.

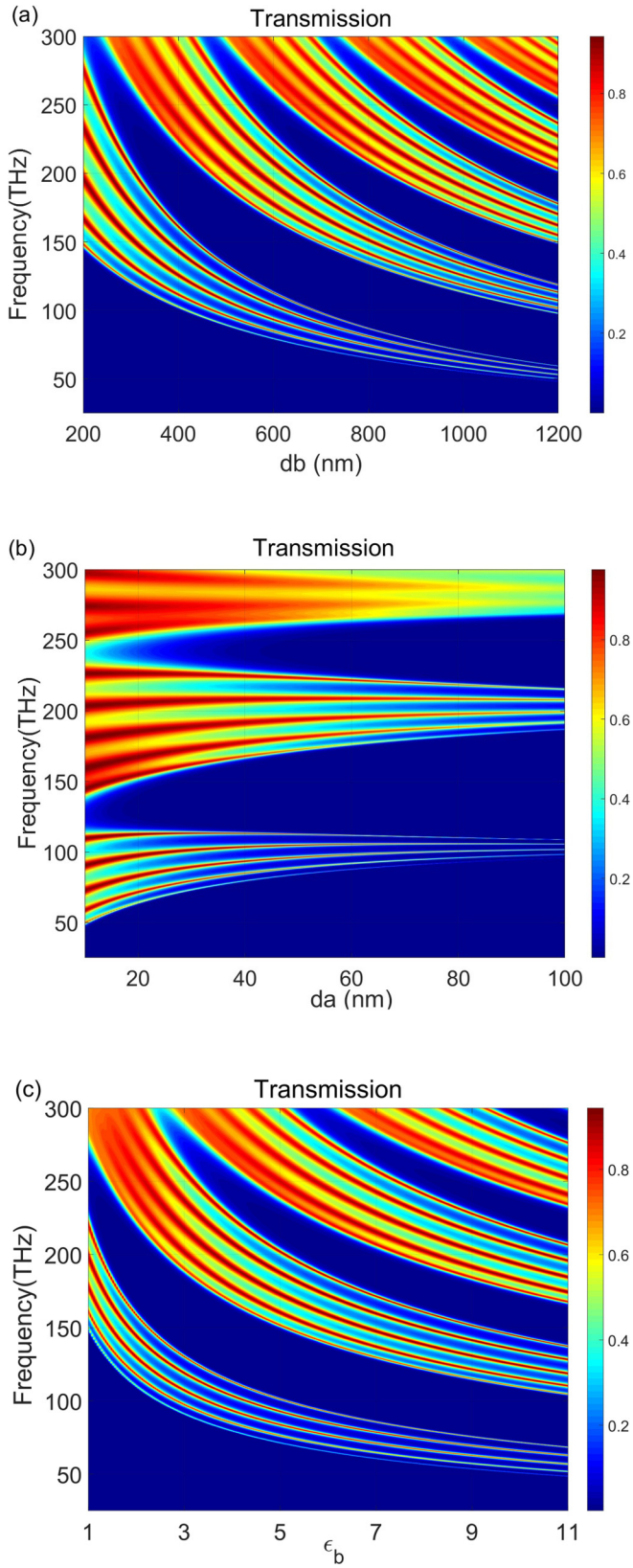

FIG. 5. (a) Transmission of the $A(BA)_5$ stack as a function of thickness d_b of Ca_2N and frequency, where $d_a = 40$ nm. (b) Transmission as a function of thickness d_b of dielectric and frequency, where $d_b = 600$ nm. (c) Transmission as a function of permittivity of dielectric and frequency, where $d_a = 40$ nm and $d_b = 600$ nm.

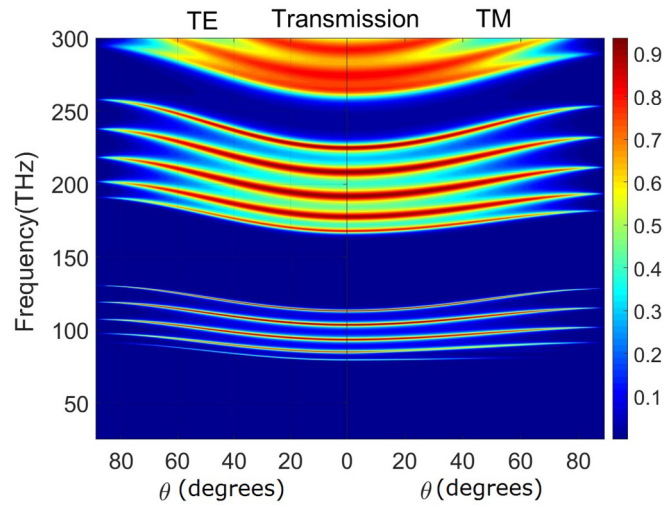

FIG. 6. Color map of the transmittance through the $A(BA)_5$ stack vs the frequency and incidence angles, with $d_a = 40$ nm and $d_b = 600$ nm; the left panel is for TE polarized waves and the right panel is for TM waves.

Figure 5(b) shows the transmission spectra when the thickness of the Ca_2N film (d_a) is tuned from 10 to 100 nm. Ca_2N films thicker than 100 nm are not considered because they block light too excessively. It is shown that as the thickness of Ca_2N film increases the transmission and the width of the passbands decrease. At the same time the high-frequency edge of the passband is not very sensitive to the thickness of d_a, while the low-frequency edge increases from 63 THz (150 THz) to 92 THz (182 THz), as d_a increases from 20 to 80 nm for the first (second) passband. The transmission spectrum as a function of incident frequency for different permittivity of the dielectric is also shown in Fig. 5(c), where $d_a = 40$ nm and $d_b = 600$ nm. It is clear that when increasing the permittivity of the dielectric more passbands and band gaps can be obtained in a certain frequency, which is similar to that in Fig. 5(a).

In this subsection, we focus our attention on the band-gap and passband properties for TE and TM polarized waves with any incidence angles. $d_a = 40$ nm, $d_b = 600$ nm, and $\varepsilon_b = 4$ are used, and the color map of the transmittance through the $A(BA)_5$ stack versus the frequency and incidence angles are plotted in Fig. 6. It is seen that the transmission properties are not polarization sensitive, but depend on the incidence angles, because the FP resonance condition changes with the incident angles. On the other hand, it is found that the first and the second band gap around 50 and 150 THz are almost omnidirectional and are also polarization insensitive. The two omnidirectional band gaps shift to the higher frequencies with little variation of the width as the incident angle increases. Especially, the first band gap is completely different from the usual all-dielectric Bragg gap which is strongly dependent on the Ca_2N layer and is suitable for the designing of omnidirectional band-gap filters in the midinfrared region.

By introducing defects into 1D PCs, single and multiple narrow frequency peaks will appear in the band gap, which is called the defect mode. The defect modes have been applied extensively in passband filters, resonant cavities, waveguides,

etc. [12,39]. Next we turn to study the localized defect modes induced by the defect layers inside the 1D electride material periodic structures. Consider one or two defect layers inserted into the finite 1D PCs with the structures of $A(BA)_3CA(BA)_3$, $A(BA)_2(CA)_2(BA)_3$, and $A(BA)_2CABACA(BA)_2$. The defect layer C was chosen to be Si_3N_4 dielectric too with different thickness d_c. Figure 7(a) shows the transmission of the single-defect and dual-defect structures at normal incidence, and the specific structures are demonstrated in the inset, where the defect layer C is denoted by yellow color. Here we just consider the second band gap around 140 THz; when a single-layer defect is introduced in the periodic structure, one transmission peak with 139.7 THz appears in the band gap (red short dotted line). For the dual-layer defect structure $A(BA)_2(CA)_2(BA)_3[A(BA)_2CABACA(BA)_2]$, two transmission peaks with $f_1 = 136.0\,\text{THz}\,(131.1\,\text{THz})$ and $f_2 = 142.3\,\text{THz}\,(147.6\,\text{THz})$ appear in the band gap (blue short dashed and green solid lines). Compared with the first $A(BA)_2CABACA(BA)_2$ defect structure, the frequency interval of the defect modes of $A(BA)_2(CA)_2(BA)_3$ is wider, which can be explained in terms of the stronger coupling effect of the respective defect mode when the two defect layers approach each other. It is also found that the single defect mode is insensitive to the location of the defect layer, while the locations of the dual defect layers affect the frequency, magnitude, and frequency interval of the defect modes remarkably.

Because the twin defect modes come from the strong-coupling effect between the respective defect modes, the transmittances will be affected by the thickness and permittivity of the defect layer. Figure 7(b) depicts the transmission spectra of the $A(BA)_2(CA)_2(BA)_3$ defective structure with different d_c, where $\theta = 0$, $d_a = 40\,\text{nm}$, and $d_b = 600\,\text{nm}$, respectively. It is seen that the twin defect modes always appear among the band gap and shift to the lower frequencies with d_c. The frequency interval of the twin defect modes is nearly the same, due to the fact that the coupling of the respective defect mode is nearly the same when the locations of the defects in the composited structure are determined. If the dielectric permittivity increases with the same d_c, similar defect modes can also be obtained. For a specific defective structure $A(BA)_2C_1AC_2A(BA)_3$, where the two defect layers are the same dielectrics with different thickness d_{c1} and d_{c2}, it is found that the twin defect modes depend on not only the defect position but also the respective thickness as shown in Fig. 7(c). The defective structure provides a way to design tunable double-channeled filters in the midinfrared region by choosing different defect dielectrics and locations. For a special application, different electrides can also be chosen, where the electride behaves with metallic character in the corresponding frequency region [4,6].

Recent theoretical calculations show that the absorption of bulk metals in the visible light region can be modulated by inserting dielectrics periodically to form a 1D PC [40]. In addition, an efficient multiband high-efficiency visible absorber can be obtained based on a 1D periodic metal-dielectric PC with a reflective substrate [14]. Here we consider an absorption structure with $(AB)_5$/Ag composed of five unit cells and a reflective silver (Ag) substrate as shown in the inset of Fig. 8, where $d_a = 40\,\text{nm}$, $d_b = 600\,\text{nm}$, and the imaginary of the dielectric is considered with $\varepsilon_b = 4 + 0.02i$. Ag substrate thickness is thick enough to block transmission, and the

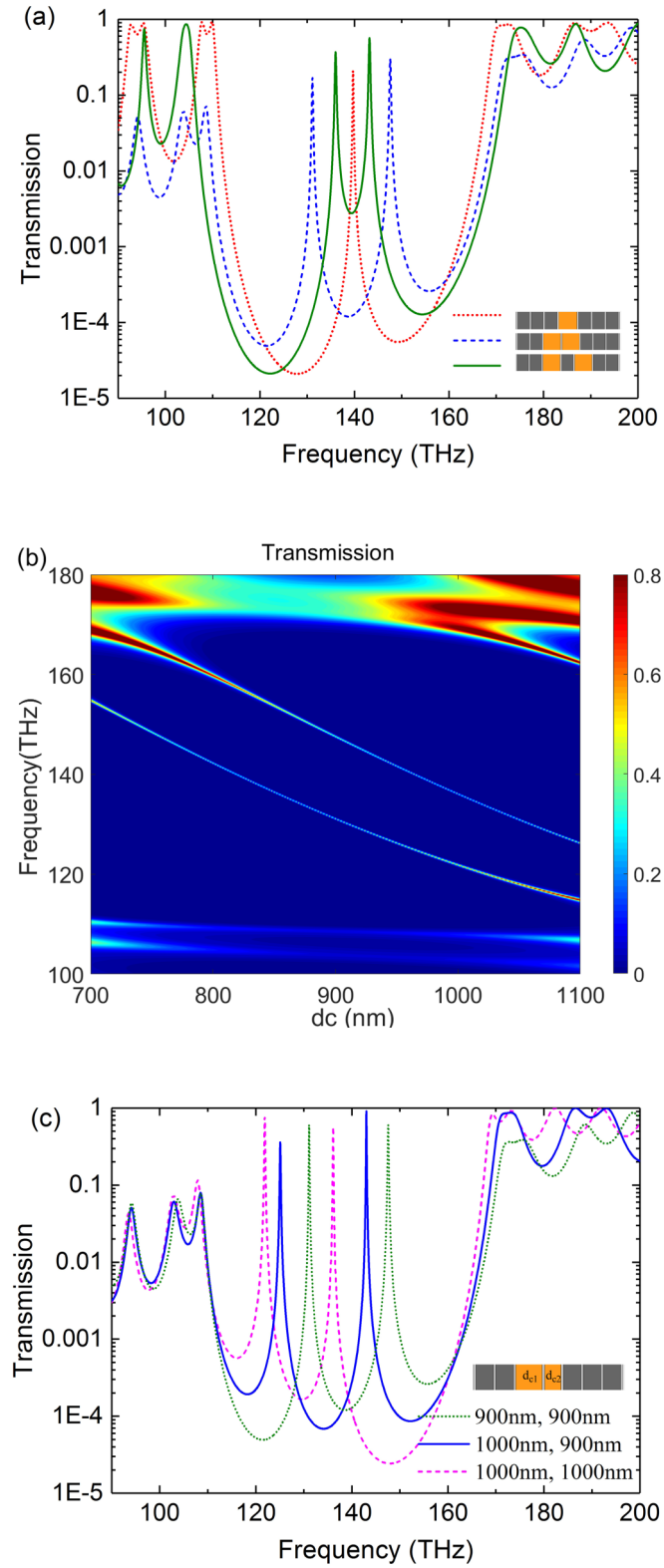

FIG. 7. (a) Transmission spectra of the defective multilayers with $A(BA)_3CA(BA)_3$, $A(BA)_2(CA)_2(BA)_3$, and $A(BA)_2CABACA(BA)_2$, where $\varepsilon_c = 4$, $d_c = 900\,\text{nm}$, and the other parameters are the same as those in Fig. 3. (b) The twin defect modes of $A(BA)_2(CA)_2(BA)_3$ as a function of frequency and the thickness of d_c under normal incidence. (c) The twin defect modes of $A(BA)_2C_1AC_2A(BA)_3$, where the thicknesses of defect layers are d_{c1} and d_{c2}, respectively.

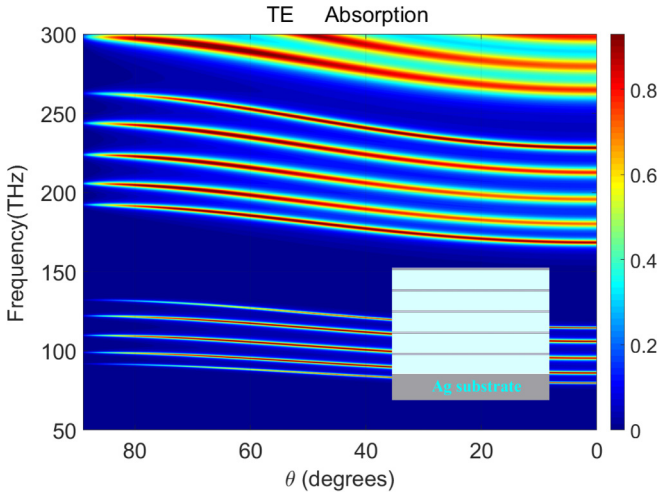

FIG. 8. Absorption of the proposed $(AB)_5$/Ag absorber as a function of frequency and the incident angles for TE polarization, where $d_a = 40\,\text{nm}$, $d_b = 600\,\text{nm}$, and $\varepsilon_b = 4 + 0.02i$.

permittivity of silver chosen is the same as that in Ref. [20]. The calculated absorption as functions of frequency and the angle of incidence is presented in Fig. 8 for TE polarization (the TM case is similar, not shown here). From the figure, it is evident that there are five absorption peaks for the five-unit-cell absorber which corresponds to the transmission peaks in Fig. 6. The absorption bandwidth in the second band is much wider than that in the first one, and all the absorption peaks are higher than 90% for normal incidence. Although the five absorption peaks blueshift with the incident angles, the absorption effect is robust, and the bandwidth and angular performance of the present structure are not very sensitive to the incident angles. The maximum absorption remains greater than 85% even for the angle of 80°. Overall, the absorption property is less sensitive to polarization and angular changes. In addition, we also found that the number of absorption peaks within each photonic band precisely corresponds to the number of unit cells because the truncated PC lattices select the resonant modes. Ca_2N is highly reactive with ambient oxygen and water vapor; for practical application, the top and bottom of the proposed structures can be covered with a SiO_2 protection layer. It is found that the enhanced transmission, field distribution, defect modes, and absorption properties are slightly affected by the existence of the protection layer.

IV. CONCLUSIONS

We study the band structures and the optical permittivity of the 2D electride Ca_2N by using DFT calculations. The significant anisotropy in the in-plane and out-of-plane permittivities was observed, which shows that Ca_2N possesses metallic behavior in the midinfrared region of interest. The enhanced transmission, field distribution, defect modes, and absorption properties of a 1D electride-dielectric PC are studied systematically. It is shown that the multilayer supports a series of passbands and stopbands, and the transmission resonances in the bandpass region are identified as coupled FP resonances associated with the individual cavities of dielectric slabs. The high- and low-frequency edges of the passband have weak dependence on the overall length of the structure, and the upper edge is determined only by the dielectric slab. The passband and stopband are nearly omnidirectional and polarization insensitive. The structures with two defects can possess twin defect modes, and the location and the frequency interval between them can be adjusted by changing the position and the thickness of the respective defect. Furthermore, multiband absorption bands are also obtained when the 2D electride PC is placed on the top of a thick metallic substrate. Compared with the conventional metal-dielectric periodic structures, where similar optical properties can hardly survive in the long-wavelength range due to the high loss, such properties of a Ca_2N PC can be used to design tunable filters and absorbers in midinfrared.

ACKNOWLEDGMENTS

L.Z. would like to thank Dr. G. Tang in the Department of Applied Mechanics, Beijing Institute of Technology for helpful advice in revising this paper. This research was supported by National Natural Science Foundation of China (Grants No. 11804081 and No. 11804082), by Natural Science Foundation of Henan Educational Committee (Grants No.15A416007, No. 15B416001, No. 19A140009, No. 182102410047, and No. NSFRF140132), by the Innovation Scientists and Technicians Troop Construction Projects of Henan Province (Grant No. CXTD2017089), and by University of Southampton Zepler Institute Research Collaboration Stimulus Fund (Grant No. 517719105) enabled by the 2017–2018 United Kingdom Higher Education Innovation Fund.

[1] J. L. Dye, Science **301**, 607 (2003).
[2] K. L. K. Daniel, L. Druffel, A. H. Woomer, F. M. Alcorn, J. Hu, C. L. Donley, and S. C. Warren, J. Am. Chem. Soc. **138**, 16089 (2016).
[3] K. Lee, S. W. Kim, Y. Toda, S. Matsuishi, and H. Hosono, Nature (London) **494**, 336 (2013).
[4] D. L. Druffel, A. H. Woomer, K. L. Kuntz, J. T. Pawlik, and S. C. Warren, J. Mater. Chem. C **5**, 11196 (2017).
[5] T. Inoshita, S. Jeong, N. Hamada, and H. Hosono, Phys. Rev. X **4**, 031023 (2014).
[6] S. Guan, S. A. Yang, L. Zhu, J. Hu, and Y. Yao, Sci. Rep.-UK **5**, 12285 (2015).
[7] S. Laref, J. Cao, A. Asaduzzaman, K. Runge, P. Deymier, R. W. Ziolkowski, M. Miyawaki, and K. Muralidharan, Opt. Express **21**, 11827 (2013).
[8] P. Li, I. Dolado, F. J. Alfaro-Mozaz, F. Casanova, L. E. Hueso, S. Liu, J. H. Edgar, A. Y. Nikitin, S. Vélez, and R. Hillenbrand, Science **359**, 892 (2018).
[9] A. H. Aly, M. Ismaeel, and E. Abdel-Rahman, Opt. Photonics J. **2**, 105 (2012).
[10] L. Zhang, G. Wang, X. Han, and Y. Zhao, Optik **127**, 2030 (2016).
[11] C. S. Kaipa, A. B. Yakovlev, G. W. Hanson, Y. R. Padooru, F. Medina, and F. Mesa, Phys. Rev. B **85**, 245407 (2012).

[12] M. A. I. F. Scotognella, Opt. Mater **72**, 403 (2017).
[13] R. V. Nair and R. Vijaya, Prog. Quant. Electron. **34**, 89 (2010).
[14] W. Wang, Y. Cui, Y. He, Y. Hao, Y. Lin, X. Tian, T. Ji, and S. He, Opt. Lett. **39**, 331 (2014).
[15] D. Qi, X. Wang, Y. Cheng, F. Chen, L. Liu, and R. Gong, J. Phys. D **51**, 225103 (2018).
[16] Z. Bushell, M. Florescu, and S. Sweeney, Phys. Rev. B **95**, 235303 (2017).
[17] C. S. Kaipa, A. B. Yakovlev, F. Medina, and F. Mesa, J. Appl. Phys. **112**, 033101 (2012).
[18] C. A. Butler, J. Parsons, J. R. Sambles, A. P. Hibbins, and P. A. Hobson, Appl. Phys. Lett. **95**, 174101 (2009).
[19] Y. R. Padooru, A. B. Yakovlev, C. S. Kaipa, G. W. Hanson, F. Medina, and F. Mesa, Phys. Rev. B **87**, 115401 (2013).
[20] L. Zhang, X. Wang, W. Qiao, J.-Y. Ou, Q. Gu, L. He, Q. Wang, Y. Zhu, and W. Li, Opt. Commun. **421**, 66 (2018).
[21] K. J. Ooi and D. T. Tan, Proc. R. Soc. A **473**, 20170433 (2017).
[22] G. Kresse and J. Furthmüller, Phys. Rev. B **54**, 11169 (1996).
[23] P. E. Blöchl, Phys. Rev. B **50**, 17953 (1994).
[24] J. P. Perdew, K. Burke, and M. Ernzerhof, Phys. Rev. Lett. **77**, 3865 (1996).
[25] S. Grimme, J. Comput. Chem. **27**, 1787 (2006).
[26] M. Methfessel and A. Paxton, Phys. Rev. B **40**, 3616 (1989).
[27] W. Ding, L. Chen, and C. H. Liang, Prog. Electromagn. Res. **70**, 37 (2007).
[28] L. Zhang, K. Fang, G. Du, H. Jiang, and J. Zhao, Opt. Commun. **284**, 703 (2011).
[29] S. Wang and L. Gao, Eur. Phys. J. B **48**, 29 (2005).
[30] J. S. Oh, C. J. Kang, Y. J. Kim, S. Sinn, M. Han, Y. J. Chang, B.-G. Park, S. W. Kim, B. I. Min, and H. D. Kim, J. Am. Chem. Soc **138**, 2496 (2016).
[31] A. Walsh and D. O. Scanlon, J. Mater. Chem. C **1**, 3525 (2013).
[32] J. Hu, B. Xu, S. A. Yang, S. Guan, C. Ouyang, and Y. Yao, ACS Appl. Mater. Inter. **7**, 24016 (2015).
[33] O. Reckeweg and F. J. DiSalvo, Solid State Sci. **4**, 575 (2002).
[34] S. Guan, S. Y. Huang, Y. Yao, and S. A. Yang, Phys. Rev. B **95**, 165436 (2017).
[35] J. Heyd, G. E. Scuseria, and M. Ernzerhof, J. Chem. Phys. **118**, 8207 (2003).
[36] N. N. Lepeshkin, A. Schweinsberg, G. Piredda, R. S. Bennink, and R. W. Boyd, Phys. Rev. Lett. **93**, 123902 (2004).
[37] L. Zhang, A. M. Agarwal, L. C. Kimerling, and J. Michel, Nanophotonics **3**, 247 (2014).
[38] C. S. Kaipa, A. B. Yakovlev, F. Medina, F. Mesa, C. A. Butler, and A. P. Hibbins, Opt. Express **18**, 13309 (2010).
[39] A. Sánchez, A. Porta, and S. Orozco, J. Appl. Phys. **121**, 173101 (2017).
[40] J. Yu, Y. Shen, X. Liu, R. Fu, J. Zi, and Z. Zhu, J. Phys. Condens. Mat. **16**, L51 (2004).